Simultaneous ranging and velocimetry with multi-tone continuous wave lidar

MUSTAFA MERT BAYER,[1] [ID] **RASUL TORUN,**[1] [ID] **XUN LI,**[1] **JOSE E. VELAZCO,**[2] **AND OZDAL BOYRAZ**[1,*] [ID]

[1]*Electrical Engineering and Computer Science Department, University of California, Irvine, CA 92697, USA*
[2]*Jet Propulsion Laboratory, Pasadena, CA 91109, USA*
*oboyraz@uci.edu

Abstract: In this paper, we demonstrate analytical modeling and experimental verification of simultaneous ranging and velocimetry measurements in multi-tone continuous wave lidars. To assess the ranging performance of the proposed lidar, a comparative experiment of the multi-tone continuous wave and time-of-flight techniques is performed. The average deviation in ranging is ~0.75cm with >90% fitting accuracy, which corresponds to the uncertainty of the time-of-flight measurements due to the detector bandwidth. Simultaneous ranging and velocimetry are performed on a moving target. The velocimetry accuracy of the multi-tone continuous wave lidar is dictated by the frequency resolution of the Doppler shift, which is measured as ± 0.8cm/s. The results indicate that multi-tone continuous wave lidars can be improved to perform remote sensing for oceanography and atmospheric sciences and for autonomous vehicles without using any amplitude, frequency or phase sweeping.

1. Introduction

Over the past years, light detection and ranging (lidar) systems have been vastly investigated and commercialized for various platforms such as self-driving cars [1], unmanned aerial vehicles and spacecraft [2]. A wide range of lidar applications such as topographical imaging [3], remote object sensing, oceanographic and atmospheric surveillance [4], navigation and driver assistance [1,5] mostly relies on range measurements. Hence, the majority of the lidar instrumentation used in these applications operate in a pulsed-mode to acquire the range information by comparing the delay between the ejection time of an optical impulse and the detection time of the backscattered light in a technique called Pulsed Time of Flight (PToF) measurements [6,7]. Inherently, this conventional approach lacks the capability of simultaneously extracting the range and velocity information of a moving target unless a post-processing algorithm on the acquired distance information is implemented [8–10]. Alternatively, the use of frequency chirped mode-locked laser pulses or modulated Q-switched pulses have been proposed to improve the capability of PToF for simultaneous ranging and velocimetry [11,12].

Continuous wave (CW) laser-based lidar systems are being investigated recently as an alternative to PToF [13–15]. CW lidars are desired because they use coherent detection techniques that provide a higher signal-to-noise ratio (SNR) than the direct detection method used in PToF. Up to date, various CW lidar techniques such as amplitude-modulated continuous wave (AMCW) lidars, frequency modulated continuous wave (FMCW) lidars, and phase-based ranging have been demonstrated by various groups [16–22]. In the AMCW, the goal is to measure the phase difference between the reference and the backscattered signal after convolution with the local oscillator, and in the FMCW, the range is measured by observing the beat note of the signal after optical heterodyning with the local oscillator. Hence, to perform these measurements and to extract the precise distance of the target, the AMCW method requires sweeping of amplitude and phase, while the FMCW technique requires frequency sweeping. In particular, FMCW lidars that

can also detect the Doppler shifts caused by moving targets, outperform the alternatives in terms of simultaneous ranging and velocimetry. Under distinct configurations, and by implementing various sweeping techniques, concurrent ranging and velocimetry capability of different FMCW lidars were previously demonstrated [23–26].

Previously, we proposed and demonstrated the multi-tone continuous wave (MTCW) lidar technique that uses a single CW laser modulated by multiple RF tones, and coherent detection for range measurements without employing any form of sweeping [27–30]. In this technique, the range is acquired by converting the time delay between the backscattered light and the local oscillator into tone-power variations via heterodyne detection. Since the detected RF tones exhibit a sinusoidal pattern based on their individually accumulated phases, and the frequency of this sinusoidal pattern is inversely proportional to the target distance, an accurate range measurement is possible from the recognition of the pattern encoded on RF tone powers. In this paper, we present the theoretical model and experimental demonstration of simultaneous ranging and velocimetry capability of the MTCW lidar technique. In particular, we show that the velocity information can be extracted by measuring the Doppler shifts induced by a moving target near the baseband in the acquired spectrum. We compare the accuracy of our range measurements with simultaneous PToF lidar data. Similarly, the velocity measurements are verified with the specs of the utilized motorized stage. We achieved ~0.75cm measured distance deviation (set by the temporal resolution of the measurement system) in between MTCW and PToF techniques, and ± 0.8cm/s velocimetry accuracy.

2. Working principle

To realize ranging in the MTCW system, a narrow-linewidth CW laser is modulated by multiple RF tones in a Lithium Niobate Mach-Zehnder modulator. RF tone frequencies are selected according to the detector bandwidth (BW). The modulated optical carrier is then brought to the free space via a collimator and a portion of the beam is separated as a local oscillator to achieve interferometric coherent detection as illustrated in Fig. 1(a). The electric field of the measurement arm, E_{meas}, is formulated in Eq. (1) by considering the transfer function of a Mach-Zehnder electro-optic modulator (MZM) under push-pull configuration.

$$
\begin{aligned}
E_{meas} = &\frac{A_0}{2\sqrt{2}}\alpha_{meas} \exp\left(j(2\pi f_0)t + j\phi_0 + j2\pi f_0\frac{2L_{meas}}{c}\right) \\
&-m\frac{A_0}{4\sqrt{2}}\alpha_{meas} \sum_{i=1}^{N} \left\{ \begin{array}{l} \exp\left[j(2\pi f_0 + 2\pi f_i)t + j(\phi_0 + \phi_i) + j(2\pi f_0 + 2\pi f_i)\frac{2L_{meas}}{c}\right] \\ + \exp\left[j(2\pi f_0 - 2\pi f_i)t + j(\phi_0 - \phi_i) + j(2\pi f_0 - 2\pi f_i)\frac{2L_{meas}}{c}\right] \end{array} \right\}
\end{aligned}
\tag{1}
$$

Here A_0 is the amplitude of the electric field, m is the modulation index of the modulator, c is the speed of the light, and α_{meas} is the linear attenuation coefficient in the measurement arm. The terms f_i and ϕ_i represent the frequency and the phase of the ith RF tone, while f_0 and ϕ_0 are the frequency and phase of the optical carrier, respectively. L_{meas} is the distance between the target and the output facet of the beamsplitter (BS). The electric field of the reference arm, E_{ref}, after the BS is identical to E_{meas}. However, the α_{meas} should be replaced with α_{ref}, A_o should be modified based on the BS ratio and the distance between the BS and the reference mirror, L_{ref}, should take place of L_{meas} to formalize E_{ref}. The photocurrent generated over the photodetector is $I_{PD} = R(E_{ref} + E_{meas})(E_{ref} + E_{meas})^*$, where R is the responsivity of the photodiode. The final delivered photocurrent, I_{PD}, by a P-I-N photodiode can be formalized as in Eq. (2) for a stationary

target without the inclusion of any velocity component [27].

$$
\begin{aligned}
I_{PD} = I_{PD,ave} &- \frac{1}{4}RmA_0^2 \sum_{i=1}^{N} (\alpha_{ref}\alpha_{meas} + \alpha_{ref}^2) \cos\left(2\pi f_i t + \frac{4\pi}{c}L_{ref}f_i\right) \\
&+ (\alpha_{ref}\alpha_{meas} + \alpha_{meas}^2) \cos\left(2\pi f_i t + \frac{4\pi}{c}L_{meas}f_i\right)
\end{aligned}
\tag{2}
$$

Here, $I_{PD,ave}$ is the average photocurrent due to the sum of all self-beating components.
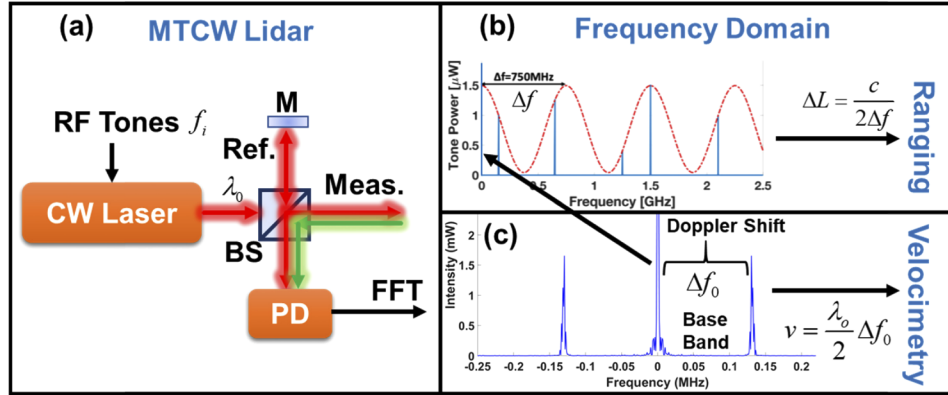

Fig. 1. (a) MTCW lidar configuration. (b) Ranging performed by the detected RF modulation tones that exhibit a sinusoidal pattern, and (c) velocimetry performed by the resultant cross beatings of the RF tones near the baseband in the frequency domain after performing FFT.

As is shown in Eq. (2), each RF tone at f_i frequency will accumulate a different phase while traveling to, and back from the target. The phase difference between the measurement and the reference arms can be expressed as $\Delta\phi = (4\pi/c)\Delta L f_i$, where $\Delta L = |L_{meas} - L_{ref}|$, after the convolution of the transmitted light with the local oscillator. It is possible to achieve ranging with $(4\pi/c)\Delta L(f_2 - f_1) = 2\pi$, where f_2 and f_1 are the two successive peak frequencies of a sine waveform. Therefore, the amplitude variations due to phase differences will yield a sinusoidal pattern in the frequency domain. Simply, the frequency of the sinusoidal fitting applied to the amplitude of the measured modulation tones will correspond to the path difference between two arms as $\Delta L = c/2\Delta f$, where Δf represents the frequency of the fitting curve as shown in Fig. 1(b). Here, the numerical solution of Eq. (2) is shown by utilizing five different RF tones up to 2.5GHz. The ΔL is set to 20cm, which yields a sine fitting with 750MHz frequency to illustrate the ranging principle of the MTCW method [27].

On the other hand, the simultaneous velocimetry is realized by exploiting the photonic Doppler velocimetry (PDV) technique [31,32]. Due to the movement of the target, the optical carrier and the modulation sidebands will experience a Doppler frequency shift in the measurement arm. The beating of the received frequency-shifted signal with the local oscillator will yield a frequency spike near the baseband as indicated in Fig. 1(c). In this process, the cross-beating terms of the RF tones in the measurement arm wouldn't overlap with the reference arm; thus, the interference will only be depending on the self-beating terms to perform ranging. The electric field of the measurement arm in Eq. (1), can be modified into Eq. (3) by introducing the Δf_0 and Δf_i, which are the Doppler shifts realized by the optical carrier and the modulation frequencies, respectively. The magnitude of the frequency shift determines the speed of the target by $v = \lambda_0 \Delta f_0/2$ or

$\Delta f_0 = 2\frac{v}{c}f_0$, where v is the speed of the target, and λ_0 is the wavelength of the optical carrier.

$$E_{meas} = \frac{A_0}{2\sqrt{2}}\alpha_{meas}\exp\left(j(2\pi f_0 + 2\pi\Delta f_0)t + j\phi_0 + j2\pi f_0\frac{L_{meas}}{c} + j(2\pi f_0 + 2\pi\Delta f_0)\frac{L_{meas}}{c}\right)$$

$$-m\frac{A_0}{4\sqrt{2}}\alpha_{meas}\sum_{i=1}^{N}\left\{\begin{array}{l}\exp\left[\begin{array}{l}j(2\pi f_0 + 2\pi f_i + 2\pi\Delta f_0 + 2\pi\Delta f_i)t + j(\phi_0 + \phi_i)\\ +j(2\pi f_0 + 2\pi f_i)\frac{L_{meas}}{c} + j(2\pi f_0 + 2\pi f_i + 2\pi\Delta f_0 + 2\pi\Delta f_i)\frac{L_{meas}}{c}\end{array}\right]\\ +\exp\left[\begin{array}{l}j(2\pi f_0 - 2\pi f_i + 2\pi\Delta f_0 - 2\pi\Delta f_i)t + j(\phi_0 - \phi_i)\\ +j(2\pi f_0 - 2\pi f_i)\frac{L_{meas}}{c} + j(2\pi f_0 - 2\pi f_i + 2\pi\Delta f_0 - 2\pi\Delta f_i)\frac{L_{meas}}{c}\end{array}\right]\end{array}\right\}$$

(3)

The interferometric coherent detection is achieved only if Δf_i is negligibly small. Such an assumption can be realized by comparing the possible Doppler shifts in the kHz-MHz range and the optical carrier frequency in the THz. Therefore, the resultant complex Doppler-shifted I_{PD} equation can be simplified by utilizing the approximation of $\Delta f_0 \pm \Delta f_i \approx \Delta f_0$. Moreover, the phase shifts of the modulation tones, ϕ_i, and the initial optical carrier phase, ϕ_0, do not affect the relative phase shift. The phase change due to the main carrier, $2\pi f_0\Delta L/c$, yields a resolution in the micrometer range and it is assumed to be averaged out by the target surface roughness and possible small optical path mismatches thus are neglected. By employing these assumptions, it is possible to simplify the resultant cumbersome I_{PD} equation that contains Δf_0 and the corresponding DC component as in Eq. (4). This is analogous to Eq. (2) if a static target is assumed with $\Delta f_0 = 0$.

$$I_{PD} = I_{PD,ave} + \frac{1}{4}RA_0^2\alpha_{ref}\alpha_{meas}\cos(2\pi\Delta f_0 t + 2\pi\Delta f_0\frac{L_{meas}}{c}) - \frac{1}{4}RmA_0^2\sum_{i=1}^{N}$$

$$\left\{\begin{array}{l}\alpha_{ref}^2\cos\left(2\pi f_i t + 4\pi f_i\frac{L_{ref}}{c}\right) + \alpha_{meas}^2\cos\left(2\pi f_i t + 4\pi f_i\frac{L_{meas}}{c}\right)\\ +\frac{1}{2}\alpha_{ref}\alpha_{meas}\left(\cos\left[(2\pi f_i + 2\pi\Delta f_0)t + 4\pi f_i\frac{L_{ref}}{c} + 2\pi\Delta f_0\frac{L_{meas}}{c}\right] + \cos\left[(2\pi f_i - 2\pi\Delta f_0)t + 4\pi f_i\frac{L_{ref}}{c} - 2\pi\Delta f_0\frac{L_{meas}}{c}\right]\right)\\ +\frac{1}{2}\alpha_{ref}\alpha_{meas}\left(\cos\left[(2\pi f_i + 2\pi\Delta f_0)t + (4\pi f_i + 2\pi\Delta f_0)\frac{L_{meas}}{c}\right] + \cos\left[(2\pi f_i - 2\pi\Delta f_0)t + (4\pi f_i - 2\pi\Delta f_0)\frac{L_{meas}}{c}\right]\right)\\ -\frac{1}{4}m\alpha_{ref}\alpha_{meas}\left(\cos\left[2\pi\Delta f_0 t + 2\pi f_i\frac{2\Delta L}{c} + 2\pi\Delta f_0\frac{L_{meas}}{c}\right] + \cos\left[2\pi\Delta f_0 t - 2\pi f_i\frac{2\Delta L}{c} + 2\pi\Delta f_0\frac{L_{meas}}{c}\right]\right)\end{array}\right\}$$

(4)

As is shown in Eq. (4), the value of Δf_0 will alter the resultant RF tone powers compared to Eq. (2). The detected tones will encounter a small reduction in power due to the power transfer to the corresponding Doppler shifts. Thus, in low SNR configurations, the impact of the noise over the RF tones will increase, which will affect the sinusoidal fitting accuracy. However, the impact of Doppler spikes will be minimal in high SNR cases in terms of sine pattern definition.

On the other hand, faster targets that can yield Doppler shifts wider than the laser linewidth (<1MHz) may inhibit performing interferometric coherent detection by creating a carrier frequency mismatch in between the E_{ref} and E_{meas} in the optical domain. Thus, for applications involving faster targets, a frequency-shifter should be integrated to the MTCW lidar to realize the interference by compensating the wide Doppler shifts, which will still enable the MTCW system to perform simultaneous ranging and velocimetry.

It is possible to extract the speed information either by applying short-time Fourier Transform (STFT) to the measured time-domain signal or by measuring the Doppler shift in the base-band after applying Fast Fourier Transform (FFT) for ranging to accelerate the data processing during the measurements. For visualization purposes, the entire flow of the MTCW lidar for simultaneous ranging and velocimetry is illustrated in Fig. 1. The time-domain data carried by I_{PD} is transferred into the frequency domain by performing FFT. First, sinusoidal fitting is applied to the acquired tone powers for ranging. Then the Doppler shift is measured from the frequency spikes near the baseband to extract the velocimetry information by using the same acquired data.

3. Methodology

The experimental setup used for ranging and velocimetry is presented in Fig. 2. To assess the accuracy of the ranging measurement and compare our results, we have implemented both

the MTCW and PToF lidars on the same platform. Here, the PToF lidar is realized by using a mode-locked (ML) laser with a 25MHz pulse repetition rate. Since our MTCW measures the delay between the reference arm and the target as amplitude variations, we use the time difference between the pulses from the reference mirror and the target mirror to capture the same information in the PToF system. A sample of PToF ranging result is presented in Fig. 3(a), where Δt represents the time difference between the pulses backscattered from the reference and the target. The path difference is further calculated via $\Delta L = c \times 2\Delta t$. The accuracy of this technique depends on the time resolution of the oscilloscope or data acquisition card, which is set to 50ps and corresponds to a 0.75cm range resolution.
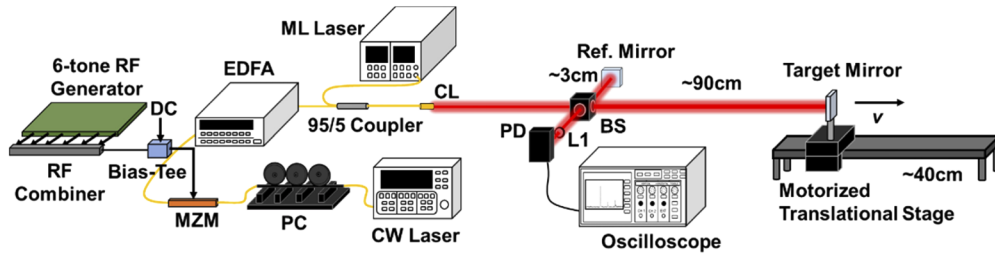

Fig. 2. The experimental setup used for MTCW and PToF lidar ranging, and simultaneous MTCW lidar ranging and velocimetry, where the target is a mirror on a motorized translational stage.
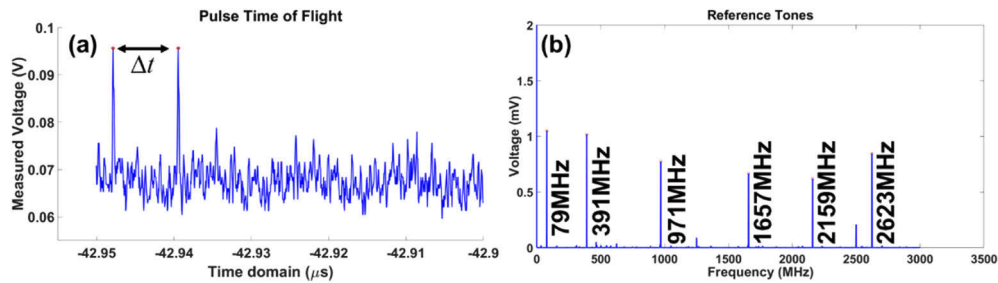

Fig. 3. (a) Performing ranging via PToF technique of a stationary target, (b) acquired reference tones for MTCW ranging.

The MTCW lidar is built by using a narrow-linewidth CW laser (<1MHz) operating at 1540.2nm with 14mW average output power that yields a coherence length of about 150m to realize coherent detection. The light is further carried to a polarization controller (PC) by a single-mode fiber (SMF) to optimize the modulation with MZM. 6 RF tones at 79, 391, 971, 1657, 2159 and 2623 MHz were generated by generator boards and combined with a 6-channel RF combiner that is followed by a Bias-Tee with an additional 1.3V DC offset to realize quadrature bias at the MZM. To define a sinusoidal pattern at least 2 RF modulation tones are required according to the sampling theory. However, having more than 2 tones will improve the fitting accuracy if the signal is noisy. The experimental demonstration with six tones here, on the other hand, is limited by the number of input ports of the RF combiner used in the setup. Moreover, the tones are carefully selected in a fashion to forestall the cross-beating and the harmonic terms to overlap with the main modulation tones. The modulated light is amplified with a commercial Erbium-doped fiber amplifier (EDFA) with a >10dB gain to achieve a higher SNR. A 95/5 fiber Y-coupler is used to combine the 5% of the ML laser with 95% of MTCW lidar and feed it to

the collimator (CL). ML laser was only operational while ranging is performed with the PToF method.

In the free space, a 50/50 beamsplitter (BS) is placed on the optical free-space path to realize interference. A reference mirror is placed ~3cm away from the BS to reflect the beam into the BS, then to the detector for coherent detection. The detected tones in the reference arm are shown in Fig. 3(b). To inhibit any ambiguities due to tone power differences, the acquired measurement data is normalized with respect to the reference arm during each measurement to realize the variations in the tone powers.

A pre-programmed motorized translational stage that can move with a desired constant speed, v, up to ~10cm/s is anchored ~90cm away from the BS, and a mirror is stationed on the stage to be used as a target to avoid the power requirements and reduce the effect of α_{meas} for demonstration purposes. The reflected beams from both mirrors are further combined in the BS and navigated into the collection lens (L1). The collected light is compressed by L1 and sent to the free space InGaAs P-I-N photodetector (PD), which has a 5GHz BW and 80µm active area. By considering the thermal noise of the oscilloscope, the minimum resolvable power is in the µW levels with the utilized PD. The data is acquired by an 8GHz BW oscilloscope, where the time window is set to 100µs with 50ps time resolution, yielding a 10 kHz frequency resolution, which determines the limit for the velocimetry accuracy.

First, the 40cm long stage is swept in 20 steps with 10 trials per step and at each step, ranging is performed with both MTCW and PToF lidars one at a time. Then the stage is operated in the scanning mode, where the target oscillates back and forth with a constant speed to perform PDV at different speeds. Moreover, 15 different trials are performed while the target is around the midsection of the motorized stage for simultaneous ranging and velocimetry. If they operate at the same time, ML distorts the data acquired by the MTCW technique. Therefore, it is not possible to acquire the position information via PToF at the same instance of data acquisition by MTCW lidar. Due to this adverse issue, the comparison is performed only for stationary targets.

4. Results and discussion

4.1. Ranging

The PToF method results yield a total coverage of 87.7cm to 126.7cm from one facet of the stage to the other. The minimum resolvable range with the MTCW can be estimated by assuming a single sinusoidal fit in the entire frequency window as $\Delta L_{min} = c/2\Delta f_{RF}$, where $\Delta f_{RF} = f_N - f_1 \approx f_N$ is defined by the first and last RF modulation tones f_1 and f_N, respectively. The resultant ΔL_{min} with the selected RF tones is ~5.9cm. On the other hand, the maximum unambiguous range, ΔL_{max}, of the MTCW methodology can be theoretically defined by the greatest-common-divisor frequency of the selected RF modulation tones, which is 1MHz in the current setup that corresponds to ~150m [27]. Overall, the current setup is capable of providing the range information in between 5.9cm-150m without facing any recursion of the emerging sine pattern. During stationary target ranging, sine fitting is performed based on $a_1 \sin(b_1 f + c_1)$ function at each step after normalization with respect to the reference arm, where b_1 represents the frequency of the fitting curve, Δf. The sweeping limits for b_1 are set based on the information gathered by the PToF technique to mimic a quasi-CW operation. The average mismatch in range measurements between PToF and MTCW is measured to be ~0.75cm, where 0.75cm is also the range resolution that PToF can provide with the given RF bandwidth and the sampling rate of the system. In particular, we use a 5GHz photodetector and 8GHz oscilloscope in the experimental system along with a 20GS/s sampling rate, hence the maximum step resolution of the PToF is found to be 0.75cm. Furthermore, the resolution of the MTCW lidar is determined by how well the variations in the tone amplitudes can be detected with respect to the fine step size. This is governed by the noise over the RF modulation tones and the selected tone frequencies. Due to the behavior of cosine, the high-frequency tones will yield larger amplitude variations compared to slower frequencies.

With amplitude variations larger than the noise limit, the MTCW lidar will perform ranging with high resolution.

On the other hand, the accuracy of the MTCW lidar is governed by the quality of the sine fitting on RF tone power distribution. The detected tone powers after the interference will vary due to the amplified spontaneous emission (ASE) at the EDFA, RF source noises and detector noises. The amplitude m' of the emerging sine fitting will indicate the accuracy of the MTCW lidar technique. Higher the sine fitting amplitude m', the better matching, and detection accuracy it will produce. Here, we use the R-squared (R^2), statistical regression model, to measure the accuracy of the sine fitting algorithm, where $R^2 = 1$ depicts a perfect fitting, and $R^2 = 0$ is no correlation. The data with maximal R^2 is selected among the 10 trials at each step and compared with the corresponding PToF measurement as in Fig. 4.
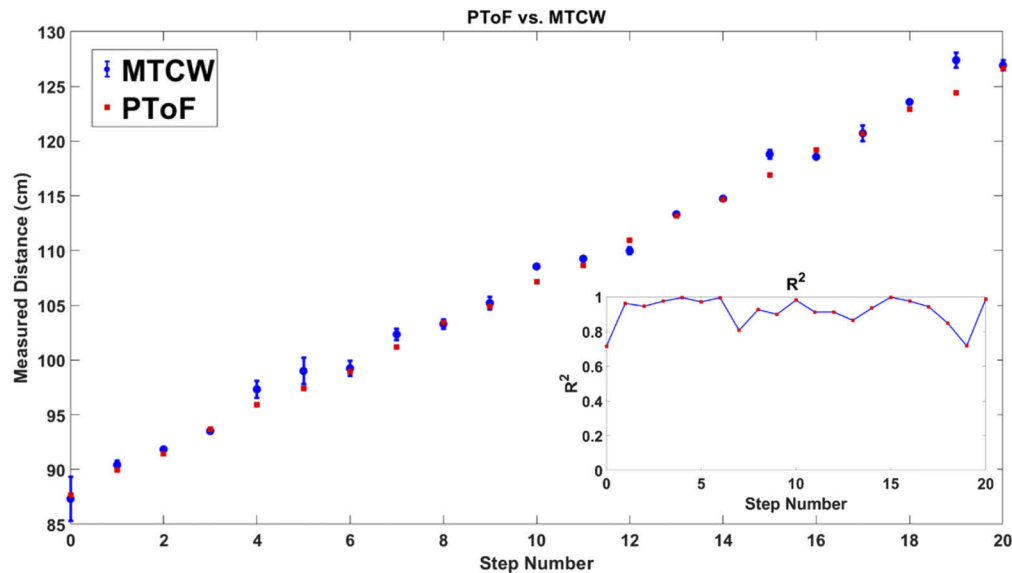

Fig. 4. Stationary target ranging with PToF technique (red) and MTCW lidar (blue) along with the corresponding error bars that represent the standard deviation of 10 trials with respect to the best R^2 data. The inset shows the calculated R^2 at the given step.

As is clear, the ranging via MTCW lidar is in a close agreement with the PToF results. The greater portion of the results is within the PToF range resolution. The maximum deviation between the two techniques is <3cm, which occurred only in the step number 19 at ~124.4cm target distance. This can be attributed to the possible destructive interferences realized by the majority of the tones at the corresponding ΔL that distorts the sine fitting algorithm, and also to the stability of RF sources. The calculated R^2 values vary between 0.715 and 0.997 and the average R^2 is 0.918, which indicates a >90% accuracy in the sine fitting algorithm. Increasing the number of RF modulation tones, or low noise RF tones may improve the variations in the R^2 measurements. The average standard deviation measured in 20 steps with 10 trials is 0.5cm, which indicates the repeatability of the MTCW methodology. Moreover, the error bars in Fig. 4 represent the standard deviation of the measurements while the target is at the same location. The largest deviation is <2cm and the smallest standard deviation is measured to be 0.12cm.

Previously, we have investigated the role of the attenuation coefficient, α_{meas}, on the amplitude of the sine fitting, m', in numerical analysis, and it is shown that in low noise systems, the sine fitting can be performed with a power imbalance up to 20dB. [27]. Based on these findings, a variable attenuator in the reference arm was suggested to preserve the m'. By introducing

monitoring power meters co-operating with a variable attenuator to the reference branch, it is possible to manipulate the power of the local oscillator depending on the collected power from the target. Hence, a coarse adjustment on the reference power will be sufficient to achieve the power balance. Otherwise, the reference arm dominates the interference and minimizes the amplitude variations induced by the phase difference. However, the effect of the noise was neglected in the former study. We performed a numerical simulation by using RSoft's OptSim$^{©}$ optical simulation software to analyze the impact of noise on m'. 6 RF tones up to 3.5GHz were used to modulate a 20mW, 1kHz linewidth input laser operating at 1550nm. The modulated light is amplified up to 1W average output power via an EDFA. In the free space, a time delay that corresponds to a 1m path difference was placed in the measurement side, while the reference arm is kept as a local oscillator after a 50/50 BS. The detection is realized via a P-I-N PD with 5GHz BW that has $R = 0.9$A/W and a dark current equal to 1.5nA, which matches the specs of the detector used in the experiment. The PD is terminated by a 50Ω load, and room temperature is assumed without any electrical amplifier gain as the parameters for the thermal noise. All the electrical and optical noises were enabled during the simulations in noise-included trials. Both measurement and reference arms were multiplied by the same linear attenuation coefficient to mimic the behavior of a variable attenuator. With this approach, the effect of the single-arm attenuation was isolated to see the impact of the noise alone. The resultant RF tones with noise after each simulation were compared with the ideal noiseless RF tones. The ideal case yields the best achievable m' that corresponds to maximal measurement accuracy. The deviation in the amplitude of the sine fitting, $\delta m'$, can be represented as $\delta m' \sim \langle \sum_i |P_{ideal}(f_i) - P_{result}(f_i)| \rangle$, where P_{ideal} and P_{result}

are the tone powers at i^{th} tone frequency under noiseless and noisy configurations, respectively. The relative $\delta m'$ is presented in Fig. 5 along with the corresponding average received powers at different attenuation levels. The average noise power is calculated to be -73dBm, where the noise equivalent power (NEP) is calculated to be 0.6fW/Hz$^{1/2}$, which matches commercially available PIN PDs.
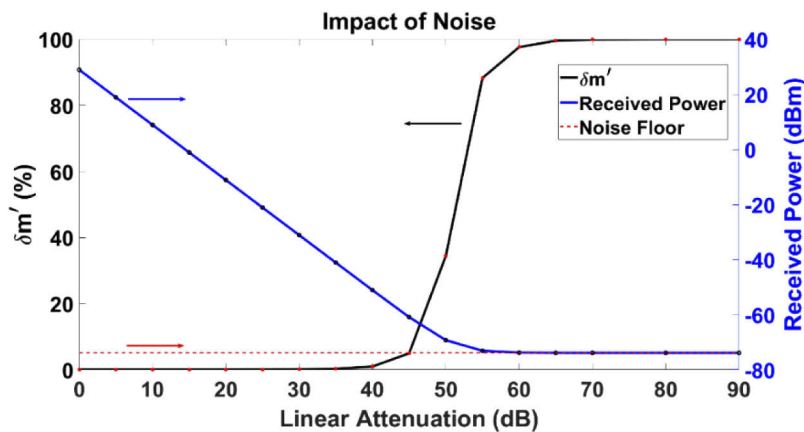

Fig. 5. The deviation in the amplitude of the sine fitting (m') due to noise (left). The received power with respect to the introduced linear attenuation (right). The noise floor is indicated as -73dBm (right).

$\delta m'$ develops an understanding of the relation between the error in the measurement due to noise and the minimum required power in detection. When the received signal power falls under -50dBm, fluctuations in the tone powers due to noise will alter the sine fitting. Therefore, the measured sine frequency will change, and the accuracy will start to degrade. It is not possible to explicitly differentiate the signal after -60dBm of received power. The largest contribution to

noise is caused by the thermal noise, which is further enhanced with the wide BW requirements. Once the effect of α_{meas} and noises are combined, received power should be high enough to achieve an SNR of >15dB. To mitigate such an issue, quasi-CW pulsation can be realized by introducing applicable repetition rates and duty cycles via the addition of another modulator. As a result, the detected power will be higher, and the RF tone powers will yield the desired sine fitting.

4.2. Velocimetry

At first, to investigate the PDV with the MTCW setup, only velocimetry is performed without simultaneous ranging. Four different velocity settings are introduced to the motor one at a time to realize four different speeds and corresponding Doppler shifts. Hence, each velocity setting yields a different frequency spike near the modulation tones and the baseband. For instance, an RF modulated optical carrier at f_0 and sidebands at $f_0 \pm f_i$ will move to new frequencies at $f_0 + \Delta f_0$ and $f_0 \pm f_i + \Delta f_0$, respectively. We use the new beating tones to estimate the velocity of the moving object.

Figure 6 presents the measured Δf_0 near the baseband under different motor velocity settings. The measured frequencies are at 45, 65, 105 and 135kHz, respectively, and the corresponding calculated speeds are 3.5, 5.0, 8.0 and 10.4cm/s. The measured speeds are verified coarsely by timing the movement of the translational stage and further confirmed with the specs of the electric motor. The accuracy of the velocimetry is related to the frequency step size, which is 10kHz. Depending on the sampling of the Doppler shift, there is an error range of about ± 0.8cm/s during the PDV.
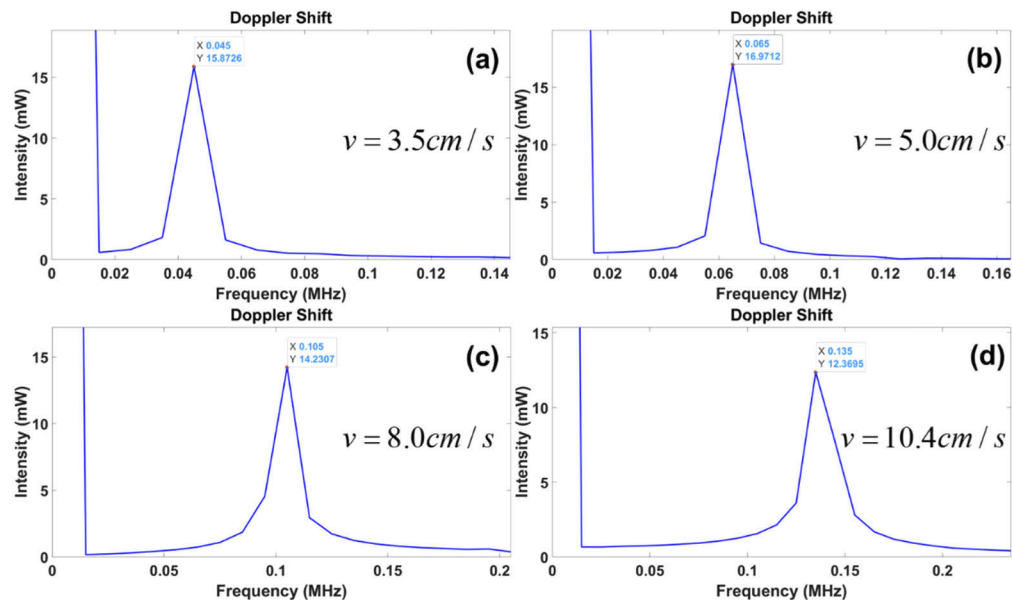

Fig. 6. Frequency spikes at the base band for moving targets with speeds of (a) 3.5 cm/s, (b) 5.0 cm/s, (c) 8.0 cm/s and (d) 10.4 cm/s. The corresponding Doppler shifts are 45kHz, 65kHz, 105kHz and 135kHz, respectively.

Due to the employed dual-sideband (DSB) modulation, coherent detection will yield both positive and negative terms caused by the Doppler shift in the RF domain as given in Eq. (4). Hence, a standard modulation technique will not resolve the direction of the motion. In order to resolve the direction, a single-sideband (SSB) modulation should be considered. During the SSB

modulation, the direction in the shifts near the modulation frequencies will reveal the direction of the speed in the RF domain as $f_i + \Delta f_0$ or $f_i - \Delta f_0$. The magnitude of the velocity can still be acquired by the Doppler spike near the baseband; however, the sign of the Doppler shift can only be realized near a modulation tone under SSB configuration. In addition, for the targets with acceleration, STFT methodology can be employed to map the changes in the speed of the target during selected time intervals [30].

4.3. Simultaneous ranging and velocimetry

Simultaneous ranging and velocimetry are performed while the target is passing through the midsection of the translational stage at ΔL of 106-110cm for verification purposes. We collect 15 data points, and present corresponding simultaneous range and velocity measurement result in Fig. 7. As expected, the measured ΔL are within the indicated range with high R^2 values in each trial. The lowest R^2 is 0.88 and the average R^2 is 0.96 that indicates the accuracy of the sine fitting. The power transferred to the Doppler spikes from the measured RF tones has a lower impact on the resultant R^2 in our experimental setup. Thus, the average R^2 is found to be within the same range of the average R^2 acquired in the static target case.
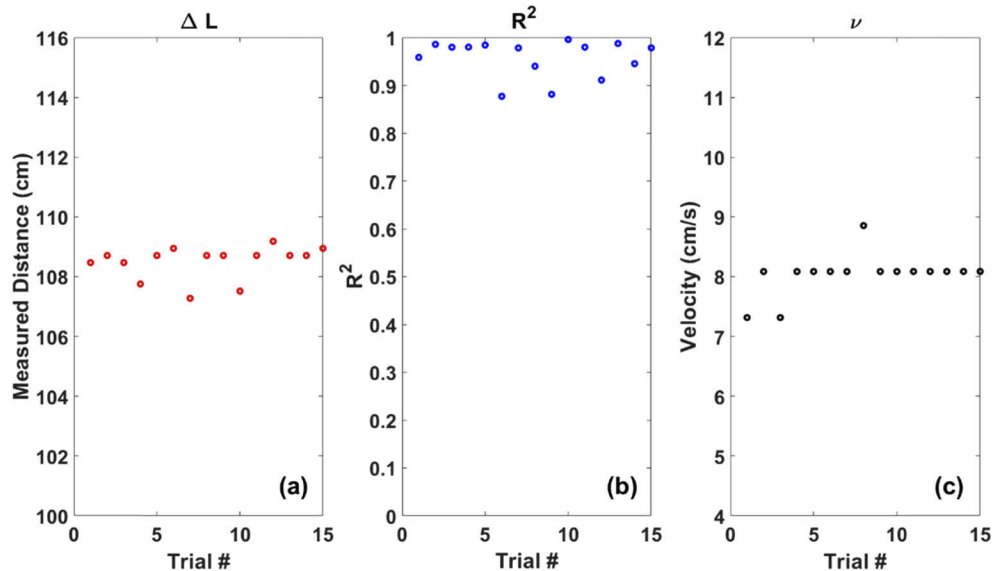

Fig. 7. Simultaneous ranging and velocimetry result for 15 trials while the target is moving with $v = 8$ cm/s. (a) Ranging, (b) corresponding R^2 of the sine fitting, and (c) the measured velocity at the same instance.

The measured frequency spikes near the baseband after coherent heterodyning is ~105kHz, which corresponds to a speed of ~8 cm/s. The majority of the trials yield the expected value except for trial numbers 1, 3 and 8. As is seen in Fig. 7(c), the outliers are within the predicted error range of ± 0.8cm/s. The sampling of the frequency spikes depicts the accuracy; thus, it is possible to improve the velocity resolution by increasing the time window without changing the sampling rate. This will result in compromising from the BW based on the requirements of the desired application.

5. Conclusion

In this work, the theoretical model of the simultaneous ranging and velocimetry of the MTCW lidar is developed. The system is demonstrated in the experimental domain by utilizing a

motorized translational stage and a target mirror under stationary and dynamic conditions. Application of the MTCW method via sine fitting yields the range information, while the Doppler shift generates the speed of the target with the RF tone beatings. The MTCW ranging results are in satisfactory correlation with the PToF measurements for stationary targets based on the R^2 analysis that yields an average deviation of ~0.75cm that corresponds to the PToF ranging resolution. Simultaneous velocimetry produces precise results within ± 0.8cm/s speed resolution.

The ranging accuracy is SNR dependent, while the resolution of the velocimetry is governed by the time window and sampling rate. The results of the numerical simulation were presented to show the impact of noise over the detected RF tones. A minimum of -60dBm received signal power is essential to resolve the detected tone powers. To realize a higher SNR, a quasi-CW pulsation can be introduced to the modulated CW laser that will have a higher peak power. However, the velocity resolution will decrease accordingly due to the decrement in the time window. Depending on the selected measurement ranges and resolution requirements for ranging and velocimetry, the quasi-CW pulse width can be carefully engineered by time gating with an additional modulator. In addition, for longer range applications that exceed the maximum unambiguous measurement range of the MTCW system, the use of quasi-CW signals with RF modulation will yield the coarse range measurement from PToF data, while the MTCW methodology yields the fine resolution information. Moreover, the linewidth of the CW laser will indicate the coherence length of the propagating beam. To realize coherent detection via interferometry, the linewidth should be selected according to the desired measurement range.

Funding

Disclosures

The authors declare that there are no conflicts of interest related to this article.

References

1. W. Zhang, "Lidar-based road and road-edge detection," in IEEE Intelligent Vehicles Symposium (IEEE, 2010), pp. 845–848.
2. L. Wallace, A. Lucieer, C. Watson, and D. Turner, "Development of a UAV-LiDAR system with application to forest inventory," Remote Sens. **4**(6), 1519–1543 (2012).
3. J. L. Bufton, J. B. Garvin, J. F. Cavanaugh, L. A. Ramos-Izquierdo, T. D. Clem, and W. B. Krabill, "Airborne lidar for profiling of surface topography," Opt. Eng. **30**(1), 72–79 (1991).
4. R. H. Couch, C. W. Rowland, K. S. Ellis, M. P. Blythe, C. R. Regan, M. R. Koch, C. W. Antill, W. L. Kitchen, J. W. Cox, and J. F. DeLorme, "Lidar In-Space Technology Experiment (LITE): NASA's first in-space lidar system for atmospheric research," Opt. Eng. **30**(1), 88–96 (1991).
5. J. Liu, Q. Sun, Z. Fan, and Y. Jia, "TOF lidar development in autonomous vehicle," in IEEE Optoelectronics Global Conference (IEEE, 2018), pp. 185–190.
6. J. Lee, Y.-J. Kim, K. Lee, S. Lee, and S.-W. Kim, "Time-of-flight measurement with femtosecond light pulses," Nat. Photonics **4**(10), 716–720 (2010).
7. S. Schuon, C. Theobalt, J. Davis, and S. Thrun, "Lidarboost: Depth superresolution for tof 3d shape scanning," in IEEE Conference on Computer Vision and Pattern Recognition (IEEE, 2009), pp. 343–350.
8. R. Armstrong, J. B. Mason, and T. Barber, "Detection of atmospheric aerosol flow using a transit-time lidar velocimeter," Appl. Opt. **15**(11), 2891–2895 (1976).
9. J. W. Bilbro, "Atmospheric laser Doppler velocimetry: an overview," Opt. Eng. **19**(4), 194533 (1980).
10. M. Gupta, A. Velten, S. K. Nayar, and E. Breitbach, "What are optimal coding functions for time-of-flight imaging?" ACM Trans. Graph. **37**(2), 1–18 (2018).
11. M. U. Piracha, D. Nguyen, I. Ozdur, and P. J. Delfyett, "Simultaneous ranging and velocimetry of fast moving targets using oppositely chirped pulses from a mode-locked laser," Opt. Express **19**(12), 11213–11219 (2011).
12. M. Vallet, J. Barreaux, M. Romanelli, G. Pillet, J. Thévenin, L. Wang, and M. Brunel, "Lidar–radar velocimetry using a pulse-to-pulse coherent rf-modulated Q-switched laser," Appl. Opt. **52**(22), 5402–5410 (2013).
13. P. F. McManamon, *LiDAR Technologies and Systems* (SPIE Press, Bellingham, WA, 2019).
14. C. V. Poulton, A. Yaacobi, D. B. Cole, M. J. Byrd, M. Raval, D. Vermeulen, and M. R. Watts, "Coherent solid-state LIDAR with silicon photonic optical phased arrays," Opt. Lett. **42**(20), 4091–4094 (2017).

15. B. Behroozpour, P. A. Sandborn, M. C. Wu, and B. E. Boser, "Lidar system architectures and circuits," IEEE Commun. Mag. **55**(10), 135–142 (2017).
16. A. D. Payne, A. A. Dorrington, M. J. Cree, and D. A. Carnegie, "Improved measurement linearity and precision for AMCW time-of-flight range imaging cameras," Appl. Opt. **49**(23), 4392–4403 (2010).
17. D. J. Lum, S. H. Knarr, and J. C. Howell, "Frequency-modulated continuous-wave LiDAR compressive depth-mapping," Opt. Express **40**(1), 10 (2001).
18. M.-C. Amann, T. M. Bosch, M. Lescure, R. A. Myllylae, and M. Rioux, "Laser ranging: a critical review of unusual techniques for distance measurement," Opt. Eng. **40**(1), 10 (2001).
19. R. D. Peters, O. P. Lay, S. Dubovitsky, J. Burger, and M. Jeganathan, "Design considerations and validation of the MSTAR absolute metrology system," in *Interferometry XII: Techniques and Analysis* (International Society for Optics and Photonics, 2004), Vol. 5531, pp. 32–44.
20. N. R. Newbury, "Searching for applications with a fine-tooth comb," Nat. Photonics **5**(4), 186–188 (2011).
21. P. Adany, C. Allen, and R. Hui, "Chirped lidar using simplified homodyne detection," J. Lightwave Technol. **27**(16), 3351–3357 (2009).
22. P. Trocha, M. Karpov, D. Ganin, M. H. Pfeiffer, A. Kordts, S. Wolf, J. Krockenberger, P. Marin-Palomo, C. Weimann, and S. Randel, "Ultrafast optical ranging using microresonator soliton frequency combs," Science **359**(6378), 887–891 (2018).
23. S. Kakuma, "Frequency-modulated continuous-wave laser radar using dual vertical-cavity surface-emitting laser diodes for real-time measurements of distance and radial velocity," Opt. Rev. **24**(1), 39–46 (2017).
24. Z. Xu, L. Tang, H. Zhang, and S. Pan, "Simultaneous real-time ranging and velocimetry via a dual-sideband chirped lidar," IEEE Photonics Technol. Lett. **29**(24), 2254–2257 (2017).
25. D. Onori, F. Scotti, M. Scaffardi, A. Bogoni, and F. Laghezza, "Coherent interferometric dual-frequency laser radar for precise range/Doppler measurement," J. Lightwave Technol. **34**(20), 4828–4834 (2016).
26. V. Vercesi, D. Onori, C. S. Arismar, A. Bogoni, and M. Scaffardi, "Tunable dual-frequency lidar exploiting a mode-locked laser for integrated coherent radar-lidar architectures," in Optical Fiber Communications Conference (IEEE, 2015), pp. 1–3.
27. R. Torun, M. M. Bayer, I. U. Zaman, J. E. Velazco, and O. Boyraz, "Realization of Multitone Continuous Wave Lidar," IEEE Photonics J. **11**(4), 1–10 (2019).
28. R. Torun, M. M. Bayer, I. U. Zaman, and O. Boyraz, "Multi-tone modulated continuous-wave lidar," Proc. SPIE **10925**, 109250V (2019).
29. O. Boyraz, M. M. Bayer, R. Torun, and I. Zaman, "TuD2.2 - Multi Tone Continuous Wave Lidar (Invited)," in *IEEE Photonics Society Summer Topical Meeting Series* (IEEE, 2019), pp. 1–2.
30. M. M. Bayer, R. Torun, I. U. Zaman, and O. Boyraz, "A Basic Approach for Speed Profiling of Alternating Targets with Photonic Doppler Velocimetry," in *Conference on Lasers and Electro-Optics, OSA Technical Digest* (Optical Society of America, 2019), p. AW4 K.4.
31. D. H. Dolan, "Accuracy and precision in photonic Doppler velocimetry," Rev. Sci. Instrum. **81**(5), 053905 (2010).
32. O. T. Strand, D. R. Goosman, C. Martinez, T. L. Whitworth, and W. W. Kuhlow, "Compact system for high-speed velocimetry using heterodyne techniques," Rev. Sci. Instrum. **77**(8), 083108 (2006).